GEOPHYSICS, VOL. 83, NO. 2 (MARCH-APRIL 2018); P. KS1–KS10, 15 FIGS., 1 TABLE.
10.1190/GEO2017-0184.1

Microseismic hydraulic fracture imaging in the Marcellus Shale using head waves

Zhishuai Zhang[1], James W. Rector[2], and Michael J. Nava[2]

ABSTRACT

We have studied microseismic data acquired from a geophone array deployed in the horizontal section of a well drilled in the Marcellus Shale near Susquehanna County, Pennsylvania. Head waves were used to improve event location accuracy as a substitution for the traditional P-wave polarization method. We identified that resonances due to poor geophone-to-borehole coupling hinder arrival-time picking and contaminate the microseismic data spectrum. The traditional method had substantially greater uncertainty in our data due to the large uncertainty in P-wave polarization direction estimation. We also identified the existence of prominent head waves in some of the data. These head waves are refractions from the interface between the Marcellus Shale and the underlying Onondaga Formation. The source location accuracy of the microseismic events can be significantly improved by using the P-, S-wave direct arrival times and the head wave arrival times. Based on the improvement, we have developed a new acquisition geometry and strategy that uses head waves to improve event location accuracy and reduce acquisition cost in situations such as the one encountered in our study.

INTRODUCTION

Hydraulic fracturing is the process of injecting fluid at pressure that exceeds the minimal principal stress of a formation to create cracks or fractures. It has been successfully used to increase permeability of unconventional reservoirs and to stimulate production of a well, and it is one of the key technologies in shale gas revolution (King, 2012). Microseismic monitoring has been widely used for hydraulic fracturing monitoring and characterization because of its initial implementation (Eisner and Le Calvez, 2007; Warpinski, 2009; Cipolla et al., 2012; Maxwell, 2014). Microseismic acquisition can use either surface or downhole deployments (Duncan and Eisner, 2010; Maxwell et al., 2010). Shallow wells (typically below the water table) are also used for situations in which downhole monitoring is inadequate (Cladouhos et al., 2013). For downhole microseismic monitoring, it is common to have only one nearby well available for microseismic monitoring (Warpinski, 2009). To assist in overcoming the aperture limitations imposed by the acquisition geometry, 3C geophones are deployed, which makes polarization analysis feasible (Yuan and Li, 2016, 2017). Moreover, multiple phase identification and full-waveform inversion of the microseismic signal are also possible in some environments (Song and Toksöz, 2011; Belayouni et al., 2015; Zhang et al., 2015).

In a borehole seismic survey, a geophone can record the ground motion accurately only if it is well-coupled to the well borehole. Unfortunately, this is usually not the case due to a lack of locking force (Gaiser et al., 1988; Sleefe et al., 1995). The poor coupling may lead to severe resonance in seismic waveform and is common in microseismic surveys (Sleefe et al., 1995). Gaiser et al. (1988) conduct an experiment to study the resonance of geophones in a vertical well used for vertical seismic profiling (VSP). In their experiment, a geophone was locked in the borehole with a horizontal locking force to imitate a typical VSP condition. They find that the geophone is subject to severe resonance issues in the horizontal (radial with respect to the borehole axis) component that is perpendicular to the locking arm and the locking force direction when there are only two points of contact with the borehole well. In cases in which cylindrical geophones are deployed in horizontal wells as is common in microseismic monitoring, there is only one point of contact with the borehole wall. The only coupling force between the geophone and borehole in this situation is usually the gravitational force of the geophone. As such, the resulting waveform shows even more severe resonance due

Manuscript received by the Editor 22 March 2017; revised manuscript received 28 August 2017; published ahead of production 13 November 2017; published online 22 December 2017.
[1]Formerly University of California, Berkeley, Department of Civil and Environmental Engineering, Berkeley, California, USA; presently Stanford University, Department of Geophysics, Stanford, California, USA. E-mail: zhishuaizhang@gmail.com.
[2]University of California, Berkeley, Department of Civil and Environmental Engineering, Berkeley, California, USA. E-mail: jwrector@lbl.gov; navamj@berkeley.edu.

to the lack of locking force. Band-pass filters have been designed and applied in previous research to mitigate the effect of downhole geophone resonance (Nava et al., 2015); however, this is based on the assumption that the resonance frequency is known and is different from the microseismic spectrum.

Microseismic surveys with a single monitoring well and location estimation with only P- and S-wave arrival times result in event locations with ambiguity due to the limited coverage of acquisition geometry (Warpinski et al., 2005). An additional constraint on event location usually comes from direct P-wave polarization (Dreger et al., 1998; Eisner et al., 2009; Li et al., 2014). The 3C data are necessary for P-wave polarization direction estimation. The major challenges in using 3C data are the unknown orientation of downhole geophones, poor coupling between geophone and borehole wall, and anisotropic/multiple arrival effects in the P-wave polarization estimation (Gaiser et al., 1988; Coffin et al., 2012; Du et al., 2013; Maxwell, 2014). These challenges make the uncertainty in the P-wave polarization estimation relatively large, and they are usually a major source of microseismic event location uncertainty (Eisner et al., 2009; Maxwell, 2009). A perforation cluster, each of which usually consists of four to five shots and spread approximately at a 0.3 m (1 ft) length, can be treated as a point source and be used for geophone orientation calibration. In this paper, we refer to perforation cluster as perforation shot, which is considered infinitely small in dimension when compared with the microseismic event location uncertainty. However, depending on the stimulation design, perforation may not have been conducted or recorded by the geophones.

When the seismic source and receiver are located at nearly the same depth in low-velocity shale, head wave arrivals can often be observed (Zimmer, 2010; Coffin et al., 2012). Researchers have recognized the possible presence of a head wave before direct arrival. There are numerous examples in the crosswell (Dong and Toksöz, 1995; Parra et al., 2002, 2006) and microseismic (Maxwell, 2010; Zimmer, 2010, 2011) literature in which the head wave arrival is the first arrival. However, the head wave is often of weak amplitude, and it is commonly regarded as contamination of the direct arrival because it can affect the polarization estimation of the direct P-wave or be misinterpreted as the direct P-wave (Wilson et al., 2003). Synthetic studies using head waves have been conducted; however, there are few studies using field data on the improvement in event location obtained by using available head waves (Zimmer, 2010, 2011). Our analysis on microseismic data acquired in the Marcellus Shale shows that head waves convey useful information, and they can be used to constrain microseismic event location as a substitute for the P-wave polarization.

In this paper, we first present the theoretical background of this study. Then, we give an overview of the microseismic survey in the Marcellus Shale. After that, we present and analyze the resonance in microseismic data acquired in the downhole survey. Subsequently, we show the head waves observed in the Marcellus Shale and use them to constrain microseismic event location as a substitute for direct P-wave polarization. Finally, we propose a new acquisition geometry to improve the traditional microseismic acquisition practice based on the location accuracy improvement due to the use of head wave arrival times.

METHODS

Resonance due to poor geophone-borehole coupling

Geophone-borehole coupling is a concern in a borehole geophysics survey. The ground motion can be accurately recorded only if the geophone has no internal resonance and is well-coupled to the borehole (Gaiser et al., 1988). However, due to operational limitation, this ideal situation is usually not achieved. In a borehole seismic survey, a geophone is coupled to the borehole with a locking mechanism, which is usually a locking arm in one direction. According to Gaiser et al. (1988), in a vertical wellbore, the impulse response of a geophone is related to the contact width of a geophone with the borehole wall, the locking force, and the weight of the geophone. The resonance is usually most severe in the horizontal component that is perpendicular to the locking force direction. For a geophone placed in a horizontal well, the only coupling force between the geophone and wellbore is usually the gravitational force of the geophone itself. This can make the resonance due to poor geophone-borehole coupling even more severe.

The recorded noise-free seismogram due to a microseismic event or perforation shot can be expressed as the convolution of source wavelet, earth impulse response, and geophone response (including resonance due to poor coupling):

$$x(t) = w(t) * e(t) * r(t), \tag{1}$$

where $x(t)$ is the recorded seismogram, $w(t)$ is the source wavelet, $e(t)$ is the earth impulse response, and $r(t)$ is the receiver (geophone) response.

Its equivalent form in the frequency domain is

$$X(\omega) = W(\omega)E(\omega)R(\omega), \tag{2}$$

where $X(\omega)$, $W(\omega)$, $E(\omega)$, and $R(\omega)$ are the frequency domain representation of $x(t)$, $w(t)$, $e(t)$, and $r(t)$, respectively.

Deconvolution of microseismic signal

The effect of a receiver resonance can be attenuated with receiver channel consistent deconvolution (Claerbout, 1992; Yilmaz, 2001). The deconvolution improves the compactness of a seismic wavelet and can help in the identification of seismic phases by recovering the impulse response of the earth. Under the assumption that the impulse response of the earth $e(t)$ is random ($|E(\omega)|$ is constant in the frequency domain), the seismogram has the same amplitude spectrum $|X(\omega)|$ with the amplitude of the convolution of the source wavelet and the geophone response $|W(\omega)R(\omega)|$. An additional minimum phase assumption enables the determination of an optimum Wiener filter, which can recover the impulse response of the earth from the recorded seismogram (Yilmaz, 2001). This can be used to remove the geophone resonance and, thus, improve the identification of the multiple arrivals.

Head wave

The generation mechanism of head waves in the Marcellus can be seen in Figure 1, which is a common acquisition configuration in shales. If the velocity of a nearby layer (the Onondaga Formation in this case) is larger than the shale, and assuming the source and receiver are located in the shale, head waves will be generated when the angle of incidence is equal to a critical angle $\arcsin(V_1/V_2)$, where V_1 and V_2 are the velocities of the low- and high-velocity layers, respectively, as shown in Figure 1. The head wave will then travel along the formation interface until the point at which it refracts back to the original low-velocity layer with angle of emergence at the

critical angle. P-P-P, S-S-S, S-P-P, and P-P-S converted head waves are potentially identifiable. In practice, the three latter head waves are difficult to identify because they occur after the first arrival. In addition, a dip-slip microseismic focal mechanism that is often thought to be the dominant rock breaking mechanism will preferentially generate P-P-P arrivals (Rutledge and Phillips, 2003). The direct arrival amplitude is inversely proportional to the distance that the seismic ray traveled from the source due to geometric spreading, whereas the head wave amplitude is approximately inversely proportional to the square of this distance (Červený and Ravindra, 1971). Thus, the head wave will decay faster than the direct arrival and usually has a smaller amplitude. As in refraction seismology, although the head wave travels a longer path than the direct arrival, it arrives before the direct arrival past the crossover distance. Figure 2 shows traveltime versus source/receiver separation for the configuration in Figure 1.

Event location estimation and velocity model calibration

The velocity model calibration and microseismic event location estimation was conducted with a microseismic event location program we previously developed (Zhang et al., 2017). It aims to minimize the misfit between the observations, which include arrival times and polarization directions, and the model predictions of these observations. An objective function is minimized iteratively with a Gauss-Newton method (Zhang et al., 2017). The standard deviation of arrival-time picking uncertainties is assumed to be 1 ms for all phases, and P-wave polarization uncertainty is assumed to be 6°.

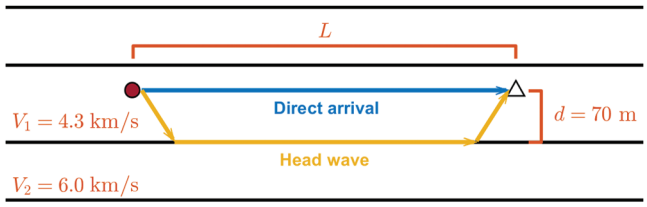

Figure 1. A common configuration for a head wave. Due to the low-velocity nature of shale, the head wave is commonly identified when there is a nearby high-velocity layer.

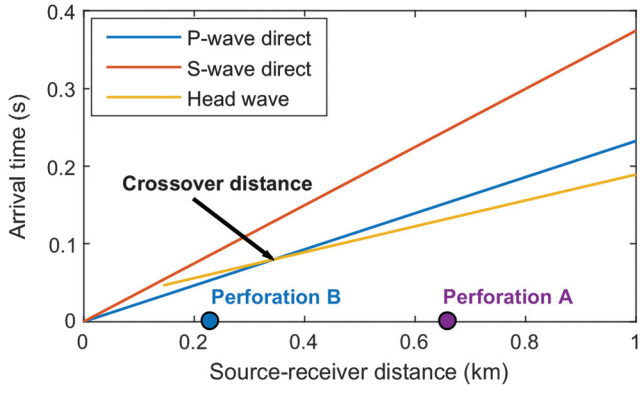

Figure 2. Arrival time of various phases as a function of the source-receiver distance. When the source-receiver distance is larger than the crossover distance, the head wave can overtake the direct arrival to be the first arrival. Perforation A and perforation B are two shots with a source-receiver distance larger and smaller than the crossover distance, respectively.

Similarly, the velocity model can be calibrated with perforation data by minimizing the objective function with respect to velocity model parameters instead of the microseismic event locations and origin times.

HYDRAULIC FRACTURING PROJECT OVERVIEW

The hydraulic fracturing project was carried out in the Marcellus Shale in Susquehanna County, Pennsylvania, within the Susquehanna River Basin. The Marcellus Shale is a Middle Devonian

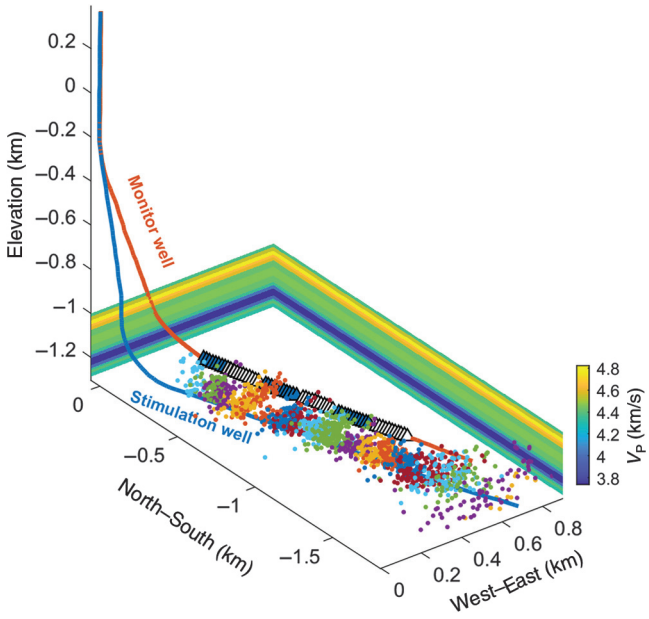

Figure 3. Microseismic survey geometry. The microseismic event locations (dots) were located conventionally using the P- and S-wave arrival times and P-wave polarization directions. The alternating white and blue geophone arrays are different locations of the same array that is used to monitor the stimulation. The stimulation stages and their corresponding geophone array positions are shown in Figure 4. Microseismic events are color coded according to their associated stimulation stages.

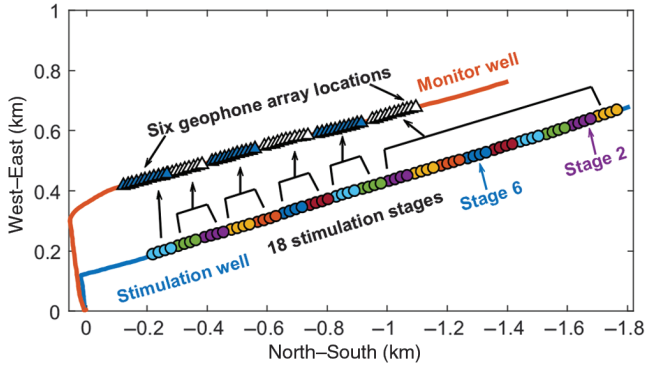

Figure 4. Map view of the acquisition geometry. The stimulation was performed in 18 stages, and the microseismic signal was recorded by an array of 11 geophones in the nearby monitoring well. The geophone array was moved according to the stimulation stage location to reduce errors due to large event to receiver distances.

age unit of marine sedimentary shale that contains largely untapped natural gas reserves. It underlies the Mahantango Formation (siltstone and shale) and overlies the Onondaga Formation (limestones and dolostones). Its natural gas trend is the largest source of natural gas in the United States. The Marcellus Shale in the studied area has a thickness of approximately 46 m (150 ft), and the average porosity and permeability are 0.08 and 600 nD, respectively.

A multiple-well pad that includes seven nearly parallel horizontal wells is the site of field acquisition (Ciezobka and Salehi, 2013). The trajectories of the lateral wells are normal to the maximum in situ horizontal stress orientation. The horizontal distances between two nearby lateral wells are approximately 152 m (500 ft), and the average horizontal wellbore length is 1109 m (3640 ft). The true vertical depths (TVDs) of the wells are approximately 1981 m (6500 ft). The target zone of the wells lies along the lower portion of the Marcellus Shale. One of the major purposes of the hydraulic fracturing project was to evaluate the potential to increase stimulation efficiency (increased production, reduced water consumption per unit of gas produced, and reduced environmental footprint) by varying the pump rate. Microseismic data have been acquired and analyzed. Surface microseismic tools were deployed in an approximately 7.8 km^2 (3 mi^2) area, and 93 stimulation stages were monitored. Downhole geophones were placed in one of the horizontal wells, and 62 stimulation stages were monitored. A previous study observed increased microseismicity during hydraulic fracturing in stages with frequent pump rate changes, which suggests better stimulation efficiency (Ciezobka et al., 2016).

Table 1. Number of microseismic events in each stage.

Stage	Number of events	Stage	Number of events
1	11	10	224
2	66	11	168
3	63	12	94
4	93	13	141
5	130	14	101
6	106	15	120
7	141	16	80
8	120	17	70
9	80	18	34

Our study is focused on two wells, a monitor well and a stimulation well, as shown in Figure 3. The lengths of the horizontal portion of the two wells are 1350 m (4430 ft) and 1700 m (5577 ft), respectively. And the average distance between the horizontal portions of the two wells is approximately 220 m (722 ft). The stimulation started from the toe and goes until the heel of the stimulation well. It consists of 18 stages with an interval of 91 m (300 ft) as shown in Figure 4. We refer to the stimulation stages as stage 1 to stage 18 from the toe to the heel of the well. Among these stages, nine were designed to have a variable pump rate and nine used the

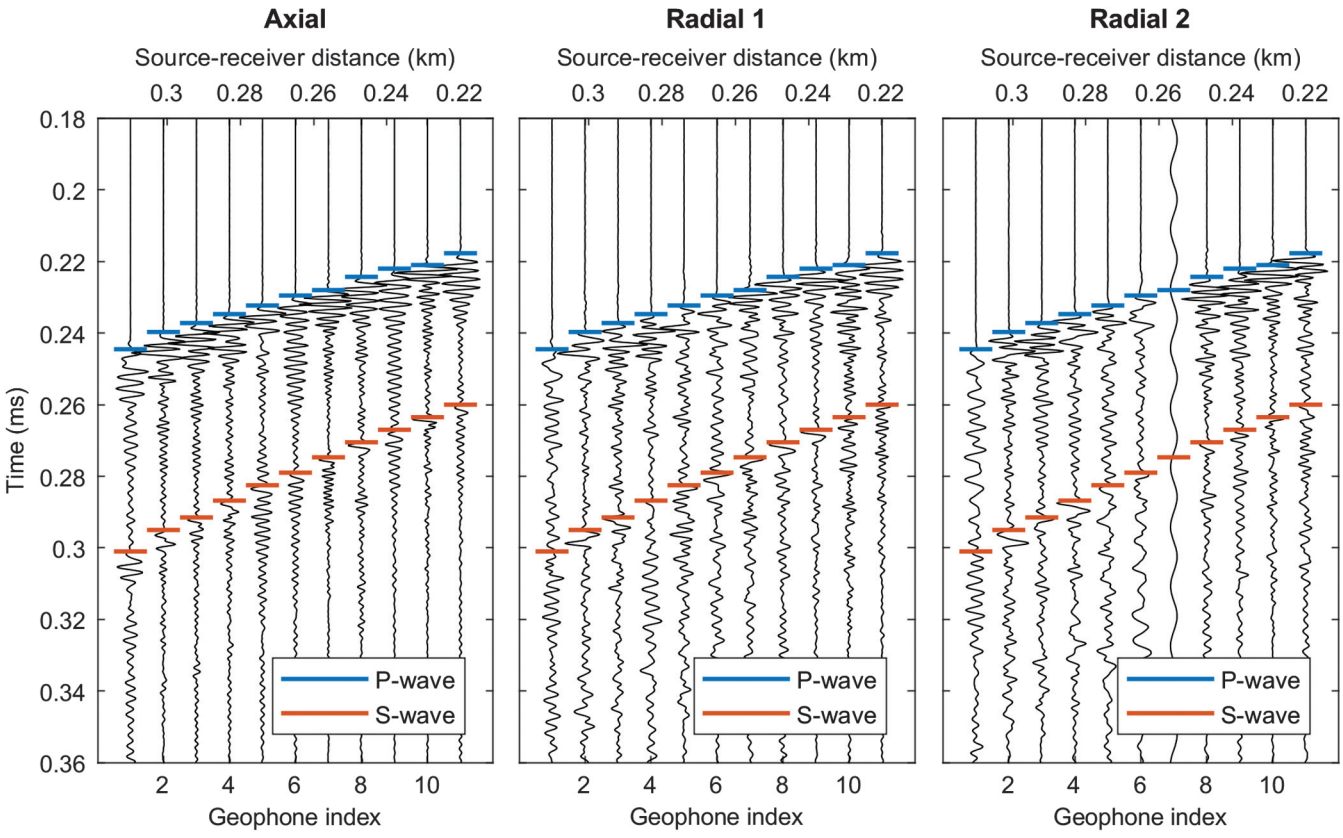

Figure 5. Waveforms of a typical perforation shot from stimulation stage 6. The waveforms of a perforation shot are usually P-wave dominated due to the source mechanism of perforation shot. A severe resonance effect in waveforms can be observed, especially in the axial component.

traditional constant-rate design. Each stage consists of four perforation shots with a perforation interval of 21 m (70 ft). We refer to the shot on the side of the toe as perforation 1 and the one on the side of the heel as perforation 4 in each stimulation stage. The fracture stages alternated along the horizontal wellbore to account for changes in the reservoir and natural fractures.

The microseismic survey was conducted with an array of 11 3C 10 Hz geophone tools. The tool spacing in the array was 15.2 m (50 ft). The geophone on the side of the toe is referred to as geophone 1, and the one on the side of the heel is referred to as geophone 11. The tools were deployed via tractor in the horizontal section of the borehole, and the only coupling between the tool and the borehole wall was due to gravity. As is typical in these types of surveys, the tool array was moved along the monitor wellbore to be roughly across from the stimulated zone in the treatment well, thereby reducing the travel path's length to improve the signal-to-noise ratio (S/N) and event location accuracy.

A total of 1842 events were detected and processed during the 18 stimulation stages. The number of events in each stage is shown in Table 1. In addition to these microseismic events, perforation shots from stages 2, 6–9, 12–14, and 17–18 were recorded by the geophone array and used for velocity model calibration and location uncertainty analysis. An isotropic 1D velocity model was created based on a sonic log from the vertical section of the stimulation well and then calibrated with perforation shots as shown in Figure 3. The geophone orientations were estimated using the P-wave polarization directions from the perforation shots. The P- and S-wave arrival times were manually picked and used for the initial microseismic event location. The P-wave polarization directions were also used to constrain microseismic event locations. The microseismic event locations obtained from this analysis are shown in Figure 3 and are color coded with their corresponding stimulation stages.

DATA ANALYSIS

Figures 5 and 6 show a typical perforation shot (the second perforation shot) and a typical microseismic event waveform from stimulation stage 6, respectively. Examination of the microseismic data acquired in this survey shows frequency resonance in the axial (with respect to the borehole) and radial components of the data. The perforation shot data are also affected by channel-dependent resonances. By visual inspection, it can be seen that the characteristic of the resonance is dependent on the channel instead of the source mechanism.

Spectrum of the resonance

The spectrum of the resonance can be seen from a short-time Fourier transform (STFT) of the 3C waveforms recorded by geophone 5 as shown in Figure 7. For the axial component, the resonance frequency is approximately 420 Hz. The first radial component has resonance frequencies of 120 and 440 Hz. The second radial component resonates at 120 and 340 Hz. Gaiser et al. (1988) show that the resonance due to poor geophone-borehole coupling is mainly on the radial component instead of the axial component. This is the char-

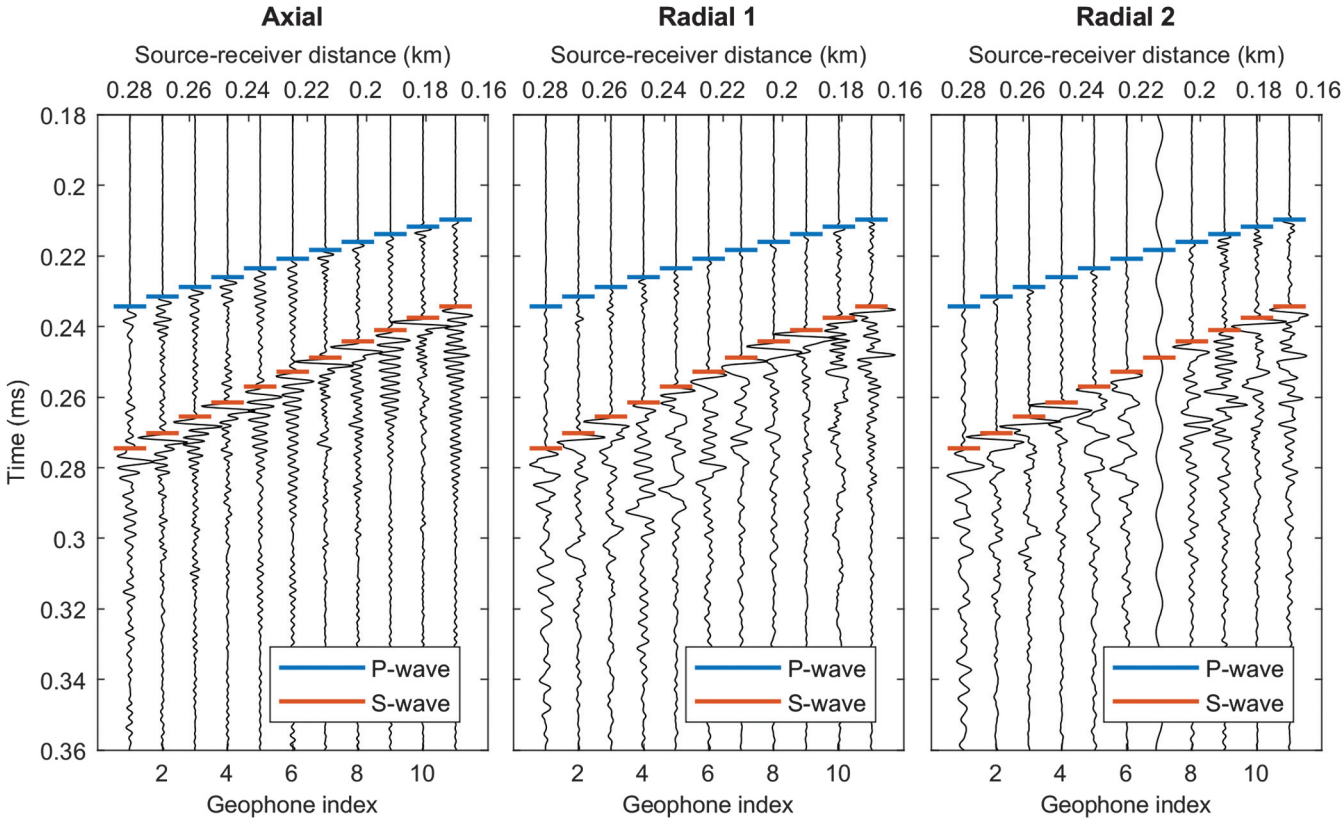

Figure 6. Waveforms of a typical microseismic event from stimulation stage 6. The waveforms of a microseismic event are usually S-wave dominated.

acter of the resonances at frequencies approximately 120 and 340 Hz. The fact that the only coupling force between the geophone and the wellbore is the gravitational force of the geophone in the horizontal well is likely the reason for the resonance in both radial components. The resonance greater than 400 Hz is polarized on the axial and the first radial components and may result from the resonance of the geophones themselves. Resonance will create problems for tasks such as Q value estimation, waveform inversion, and P-wave polarization direction estimation. In the presence of resonance, additional processing procedures should be performed such as the relative spectrum analysis introduced by Zhang et al. (2016).

Deconvolution of the microseismic signal

The presence of resonances in microseismic signals may affect the identification of seismic phases. We performed a spiking deconvolution to remove the receiver signatures in these waveforms. An optimum Wiener filter was designed using the average autocorrelation of the four perforation shots in stage 6. The waveforms before and after deconvolution are shown in Figure 8. From the comparison, we can see a significant suppression of the resonance following the P- and S-wave arrivals after the deconvolution. This suppression prevents the later phases from being contaminated by resonance due to earlier arrivals. For instance, it can be difficult to determine the S-wave arrival times on geophones 5 and 9 in Figure 8a due to their preceding resonance. After the removal of the resonance (Figure 8b), it is significantly easier to pick those arrivals on geophones 5 and 9. In addition, we also find two weak yet clear phases after the deconvolution denoted by multiple 1 and multiple 2 in Figure 8b. These two arrivals can hardly be identified in the original data.

EVENT LOCATION RESULT

Due to the azimuthal ambiguity in microseismic event location using only P- and S-wave arrival times, P-wave polarization is commonly used to constrain the azimuthal direction of microseismic events. However, the effect of resonance on the downhole geophones may result in large uncertainty in P-wave polarization estimation. In addition, the orientations of downhole geophones will require calibration using information from perforation shots, which may be unavailable. Due to the low-velocity nature of shale, the head wave is commonly identified in microseismic surveys (Maxwell, 2010; Zimmer, 2010, 2011). Like many other microseismic surveys, we observed head waves in the Marcellus Shale. Figure 9a shows the axial component of the waveforms for perforation shot 4 in stage 2 (perforation A in Figure 10). The head wave arrivals have low amplitude and high velocity moveout as annotated by the yellow picks in Figure 9a. However, as shown in Figure 9b, the waveform for perforation shot 3 in stage 6 (perforation B in Figure 10) shows no identifiable head wave because its source-receiver distance is smaller than the crossover distance. In this section, we use the head wave arrival times as a substitution for the P-wave polarization to constrain the microseismic event locations.

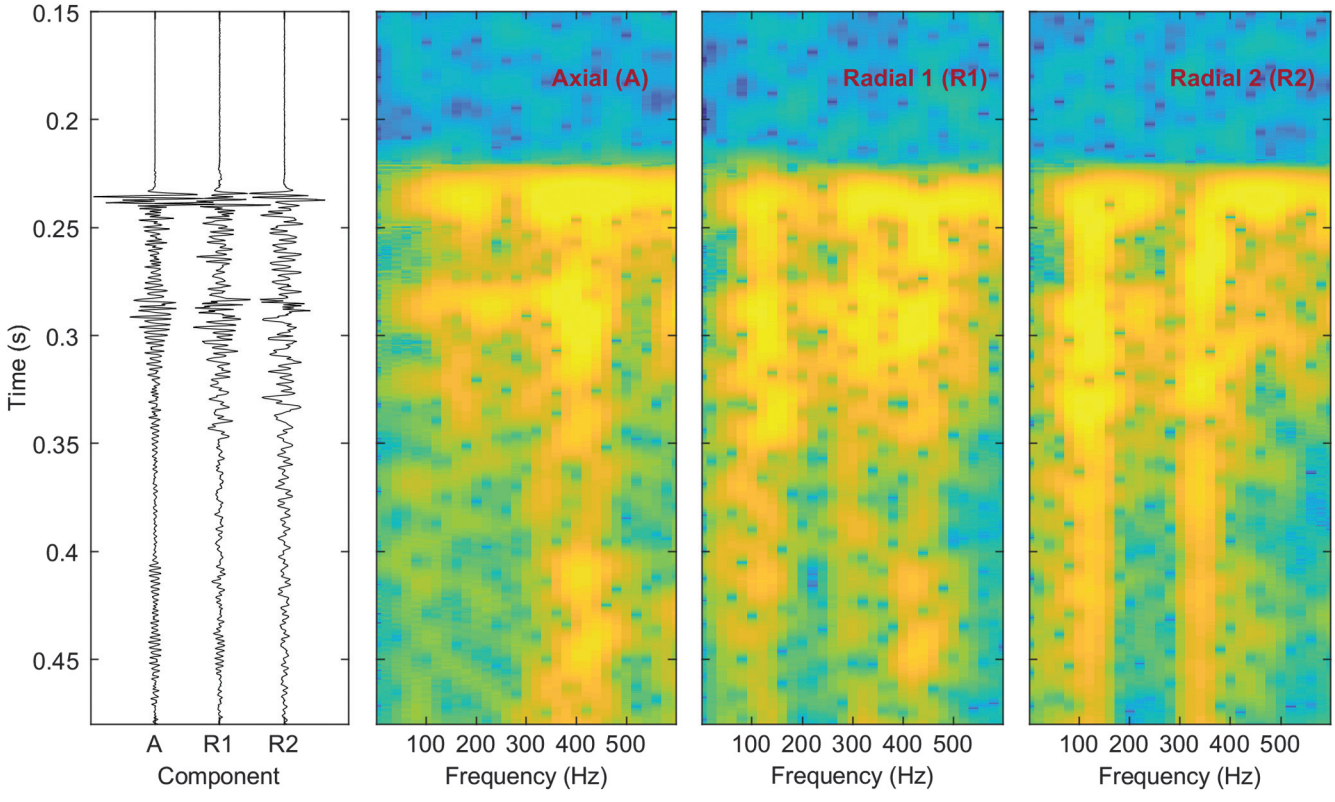

Figure 7. The STFT of a typical 3C waveform generated by a perforation shot. Yellow for high amplitude and blue for low amplitude. For the axial component, the resonance frequency is approximately 420 Hz. The first radial component has resonance frequencies of 120 and 440 Hz. And the second radial component resonates at 120 and 340 Hz. The resonance approximately 120 Hz may be due to the poor coupling between geophone and wellbore. And the resonance greater than 400 Hz may result from the geophone themselves.

For a microseismic event at a distance of L from the observation geophone array, the location uncertainty due to uncertainty in polarization will be on the order of αL, where α is the uncertainty of the P-wave polarization estimation. A common value of $\alpha = 6°$ and $L = 400$ m (1312 ft) will result in a location uncertainty of 42 m (138 ft). This is a value significantly larger than the location uncertainty resulting from the arrival-time picking uncertainty, which is usually on the order of several meters. Additional uncer-

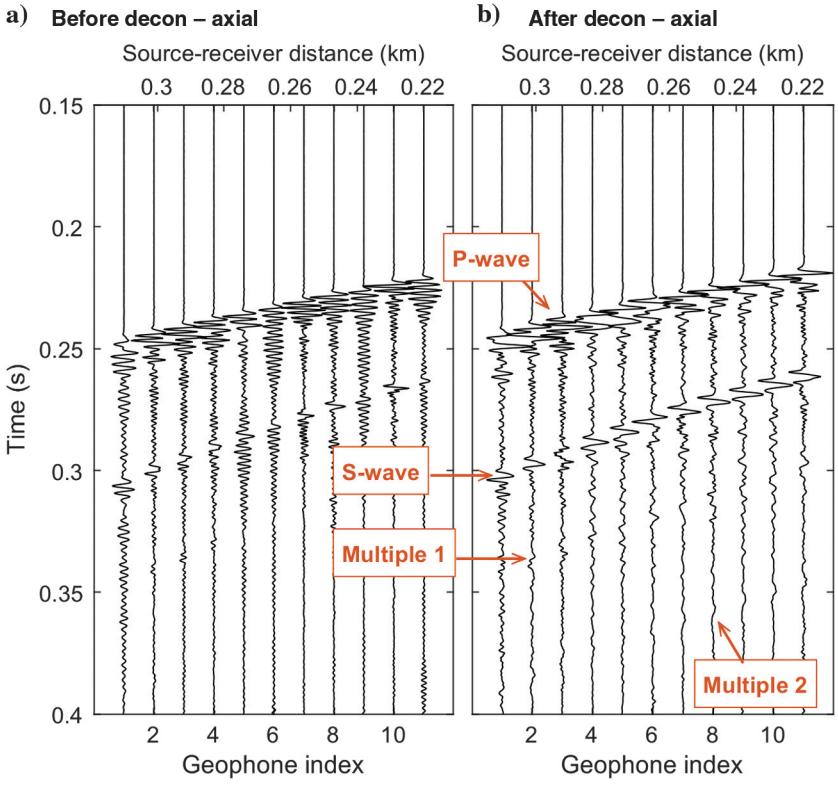

Figure 8. Deconvolution result of the axial component. The deconvolution (b) successfully suppressed the resonance in the original data (a). In addition, it enhances multiple arrivals that are hardly identified in the original waveform.

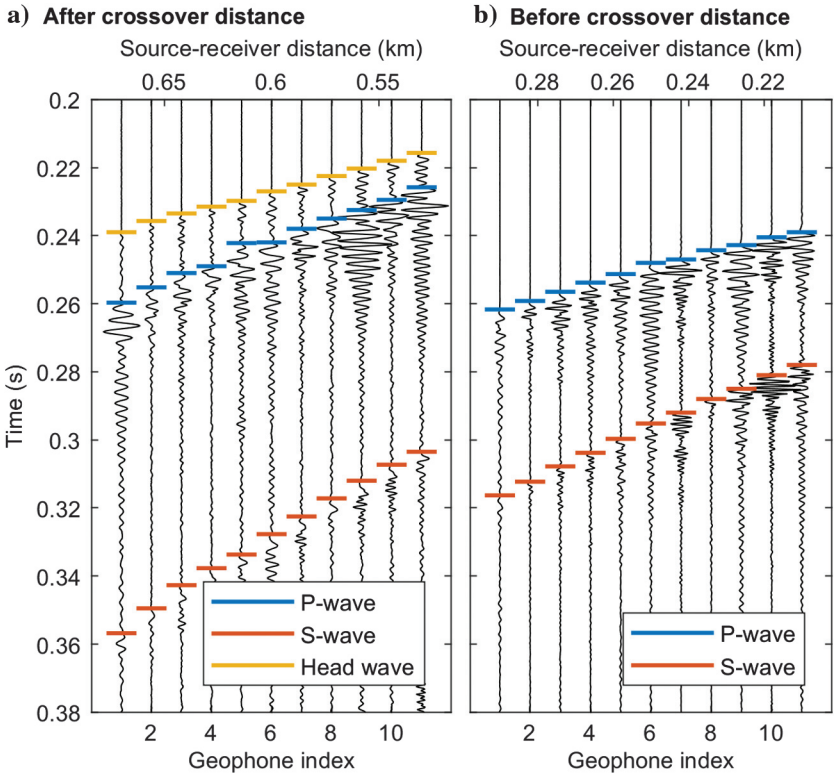

Figure 9. The axial component of the waveforms of perforation shots (a) after and (b) before the crossover distance. Head waves can be easily identified based on their low amplitude and high velocity moveout from waveform (a). The head waves arrive after the direct P-wave; thus, they cannot be identified in waveform (b). The location of the perforation shots is shown in Figure 10.

tainty usually comes from velocity model uncertainty; however, it is common for both methods.

Velocity model calibration

Because the original velocity model is based on sonic logs and calibrated with perforation shots, it is limited to the TVD of the kickoff point (sonic logs are not typically run in the horizontal section). According to this provided model, the head wave will not take over the direct P-wave to be the first arrival as observed in the waveform within the offset ranges in this study. To calibrate the velocity model, perforation shots were used and the P-, S-, and head wave arrival times were picked. From the calibrated velocity model, we found that Marcellus velocities near the stimulated interval were close to the one provided by the contractor. The calibration also reveals the existence of a high-velocity ($V_P = 6.01$ km/s) formation, the Onondaga Formation, underlies approximately 70 m (230 ft) below the geophone array. However, there was no velocity information in the original model due to the lack of sonic logs.

Finite-difference simulation

To further verify the existence of head waves and the calibrated velocity model, we conducted a finite-difference simulation to investigate the wave propagation of microseismic signals with SW4, a 3D elastic forward-modeling code (Petersson and Sjogreen, 2013). The code implements a fourth-order-accurate method in space and time. The focal mechanism of the source is assumed to be a vertical crack with a moment tensor proportional to

$$\begin{bmatrix} 1 & 0 & 0 \\ 0 & \frac{1}{\nu} - 1 & 0 \\ 0 & 0 & 1 \end{bmatrix}, \tag{3}$$

where ν is Poisson's ratio.

The source time function is assumed to be a Ricker wavelet with peak frequency at 100 Hz. The existence of head waves can be verified by the comparison between the field and synthetic waveform as shown in Figure 11. The arrival time of the head wave in field data matches that of the synthetic result well. In addition, the low amplitude ratio between P- and head wave is also verified by the synthetic simulation. The differences in the S-wave in the Vx and Vy components may be due to the lack of knowledge of source mechanism of the actual event for the finite-difference simulation.

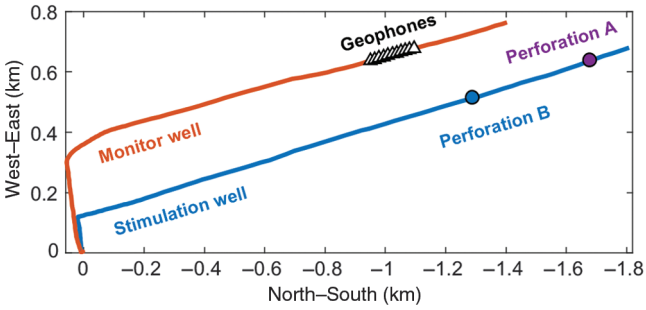

Figure 10. The locations of two perforation shots whose waveforms are shown in Figure 9.

Perforation shot location

To quantify our event location estimation uncertainty, we located the perforation shots in stage 2 with a jackknife technique (Miller, 1974). That is, for each perforation shot, its location is estimated with the velocity model calibrated with the other three perforation shots. Because the velocity model was not calibrated with the perforation shot to be located, these perforation shots in stage 2 can be treated as normal microseismic events and used for location uncertainty analysis. Our location result of the four perforation shots along with their true location is shown in Figure 12. What is also shown is the location result with the traditional method, which used direct arrivals and P-wave polarization directions.

From the comparison, we found that the method using head wave arrivals instead of P-wave polarizations gives a root-mean-square (rms) error of 19 m (62 ft), whereas the traditional method with P-wave polarizations and P-, S-wave arrival times gives an rms error of 52 m (171 ft). Given the limited acquisition geometry and relatively large source-receiver distance in this survey, the method using head wave arrival times gives a plausible result, whereas the traditional method using P-wave polarization directions leads to relatively large location uncertainty.

Relocation of events in the second stage

A map view of the microseismic event locations estimated with the traditional P-wave polarization method is shown in Figure 13. Note that the microseismic event locations in stage 2 are significantly more scattered than those in later stages. One possible explanation to this scattering is because of the larger stimulated reservoir volume associated with stage 2 stimulation. However, an alternative explanation is simply because of the larger event location uncertainties in stage 2 events due to the longer travel paths of seismic rays.

We relocated these events using direct P-, direct S-, and head wave arrivals without polarization as shown in Figure 14. The relocated events are much less scattered than the result estimated with the traditional location method. This pattern is more consistent with the microseismic event patterns in the later stimulation stages and

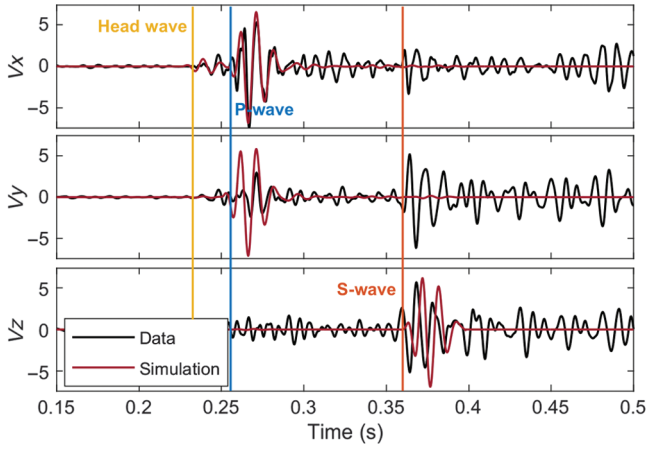

Figure 11. Comparison between a synthetic and a field waveform. The synthetic waveform matches the field data relatively well, which verifies the existence of the head wave. The difference between the S-wave in the x- and y-components may be due to the unknown source mechanism of the actual event for simulation.

indicates the effectiveness of using head wave arrival times in microseismic event locations to improve event location accuracy.

DISCUSSION

The microseismic event location methodology developed in this study relied on head wave availability. However, the head waves exist only if a high-velocity layer is present in the vicinity of the stimulation zone and the observation geophones. Even so, they can hardly be identified if they arrive after the direct arrivals, which is the case when the source-receiver distance is smaller than the crossover distance.

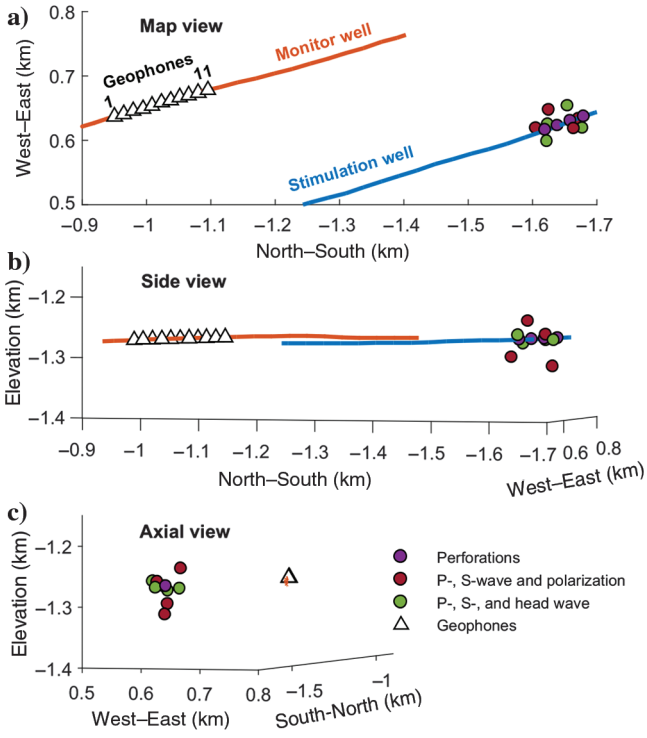

Figure 12. Comparison of estimated perforation shot locations and the true perforation locations. Location estimation using head wave arrival times gives an rms error of 19 m, whereas the traditional method using P-wave polarizations gives an rms error of 52 m.

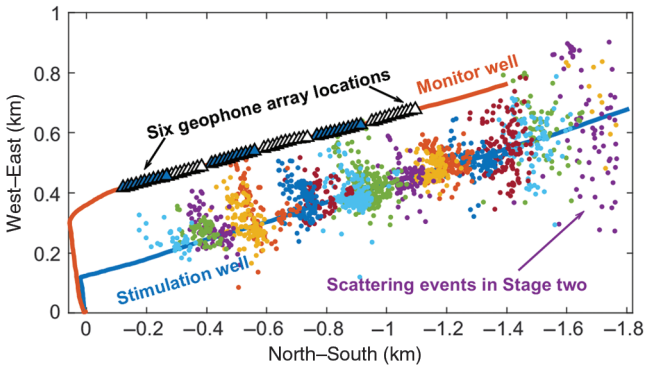

Figure 13. Map view of microseismic event locations processed using P- and S-wave arrival times and P-wave polarizations. The event locations in stage 2 are much more scattered than those in later stages.

When the source-receiver distance is smaller than the crossover distance such as the data in Figure 9b, which come from perforation shot B in Figure 10, head waves will arrive after the direct P-waves (Figure 2). In this case, it will be more difficult to pick head wave arrivals and conventional methods of event location using P-wave polarization directions may be required to constrain the event locations. Traditional acquisition practices place the geophone array as close as possible to the stimulation zone. However, our analysis shows this practice may result in a loss of information with multiple arrivals. We would propose to place the geophone array farther than a crossover distance for single horizontal well monitoring as shown in Figure 15. This acquisition geometry will enable the identification of multiple arrivals, thus improving the microseismic event location accuracy. Moreover, fewer moves (perhaps no moves whatsoever) may be required to provide accurate location information. Significant reductions in acquisition cost and wellbore risk might be achieved with this geometry without sacrificing accuracy and in some situations perhaps improved location accuracy.

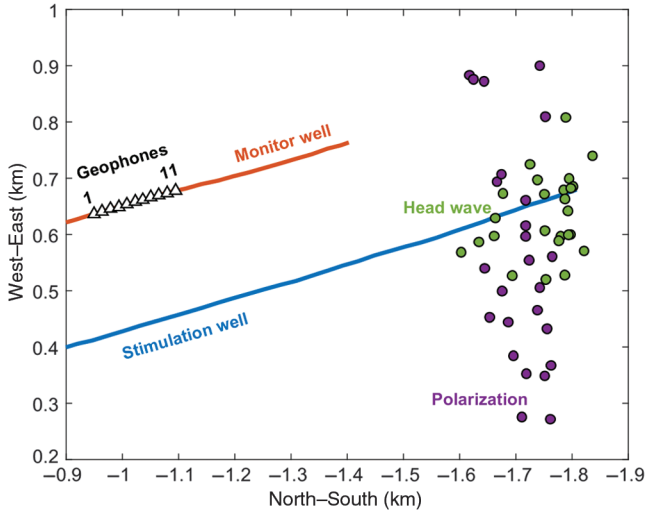

Figure 14. The microseismic event locations estimated with P-, S-, and head wave arrival times are less scattered and more consistent with other stimulation stages when compared with the microseismic event locations processed using the traditional location method.

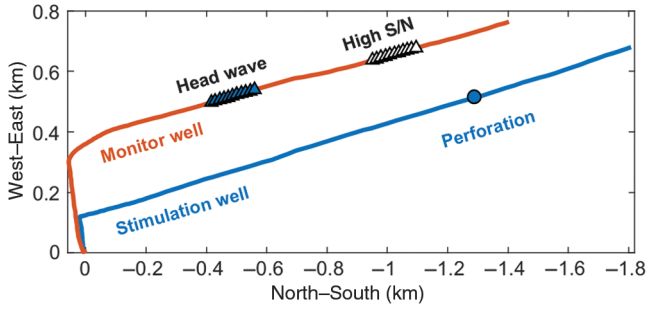

Figure 15. Traditional acquisition geometry aims at improving the S/N by decreasing the source-receiver distance (white geophone array). Our study shows that one can monitor hydraulic stimulation with a geophone array that is farther than a crossover distance (the blue geophone array) for head wave observation. This acquisition practice will be able to avoid large location uncertainty due to using P-wave polarization as well as to reduce the acquisition cost.

CONCLUSION

Resonances due to poor geophone-borehole coupling are commonly observed in a downhole microseismic survey. Deconvolution is successful in removing resonance and improves the identification of multiple arrivals. However, it will not help improve P-wave polarization estimation, which is traditionally used to constrain microseismic event location in single monitoring well observations. The existence of head waves in microseismic survey of the Marcellus Shale is observed and verified. The location result of perforation shots using the developed method verified that, whenever available and identifiable, accounting for head wave arrival time as a substitution for P-wave polarization indeed improves the microseismic location accuracy. Based on the developed method, we propose an improved acquisition geometry for single horizontal well hydraulic fracturing monitoring, which enables us to improve the identification of multiple arrivals, use the head wave as the first arrival, and improve microseismic event location accuracy as well as reduce acquisition cost.

ACKNOWLEDGMENT

The authors would like to acknowledge support from RPSEA under contract 11122-20.

REFERENCES

Belayouni, N., A. Gesret, G. Daniel, and M. Noble, 2015, Microseismic event location using the first and reflected arrivals: Geophysics, **80**, no. 6, WC133–WC143, doi: 10.1190/geo2015-0068.1.

Červený, V., and R. Ravindra, 1971, Theory of seismic head waves: University of Toronto Press.

Ciezobka, J., D. Maity, and I. Salehi, 2016, Variable pump rate fracturing leads to improved production in the marcellus shale: Presented at the SPE Hydraulic Fracturing Technology Conference, SPE 179107-MS, doi: 10.2118/179107-MS.

Ciezobka, J., and I. Salehi, 2013, Controlled hydraulic fracturing of naturally fractured shales — A case study in the Marcellus shale examining how to identify and exploit natural fractures: Presented at the SPE Unconventional Resources Conference, SPE 164524-MS, doi: 10.2118/164524-MS.

Cipolla, C., S. Maxwell, M. Mack, and R. Downie, 2012, A practical guide to interpreting microseismic measurements: Presented at the North American Unconventional Gas Conference and Exhibition, SPE 144067-MS, doi: 10.2118/144067-MS.

Cladouhos, T. T., S. Petty, Y. Nordin, M. Moore, K. Grasso, M. Uddenberg, M. Swyer, B. Julian, and G. Foulger, 2013, Microseismic monitoring of Newberry Volcano EGS demonstration: Proceedings of the 38th Workshop on Geothermal Reservoir Engineering, SGP-TR–198.

Claerbout, J. F., 1992, Earth soundings analysis: Processing versus inversion: Blackwell Scientific Publications.

Coffin, S., Y. Hur, J. S. Abel, B. Culver, R. Augsten, and A. Westlake, 2012, Beyond first arrivals: Improved microseismic event localization using both direct-path and head-wave arrivals: 82nd Annual International Meeting, SEG, Expanded Abstracts, doi: 10.1190/segam2012-1508.1.

Dong, W., and M. N. Toksöz, 1995, Borehole seismic-source radiation in layered isotropic and anisotropic media: Real data analysis: Geophysics, **60**, 748–757, doi: 10.1190/1.1443813.

Dreger, D., R. Uhrhammer, M. Pasyanos, J. Franck, and B. Romanowicz, 1998, Regional and far-regional earthquake locations and source parameters using sparse broadband networks: A test on the Ridgecrest sequence: Bulletin of the Seismological Society of America, **88**, 1353–1362.

Du, J., N. Warpinski, and C. Waltman, 2013, Anisotropic effects on polarization from highly deviated/horizontal wells in microseismic monitoring of hydraulic fractures: 83rd Annual International Meeting, SEG, Expanded Abstracts, 2008–2012.

Duncan, P., and L. Eisner, 2010, Reservoir characterization using surface microseismic monitoring: Geophysics, **75**, no. 5, 75A139–175A146, doi: 10.1190/1.3467760.

Eisner, L., P. M. Duncan, W. M. Heigl, and W. R. Keller, 2009, Uncertainties in passive seismic monitoring: The Leading Edge, **28**, 648–655, doi: 10.1190/1.3148403.

Eisner, L., and J. H. Le Calvez, 2007, New analytical techniques to help improve our understanding of hydraulically induced microseismicity and fracture propagation: Presented at the SPE Annual Technical Conference and Exhibition, SPE 110813-MS, doi: 10.2118/110813-MS.

Gaiser, J. E., T. J. Fulp, S. G. Petermann, and G. M. Karner, 1988, Vertical seismic profile sonde coupling: Geophysics, **53**, 206–214, doi: 10.1190/1.1442456.

King, G. E., 2012, Hydraulic fracturing 101: What every representative, environmentalist, regulator, reporter, investor, university researcher, neighbor and engineer should know about estimating frac risk and improving frac performance in unconventional gas and oil wells: Presented at the SPE Hydraulic Fracturing Technology Conference, SPE 152596-MS, doi: 10.2118/152596-MS.

Li, J., C. Li, S. A. Morton, T. Dohmen, K. Katahara, and M. N. Toksöz, 2014, Microseismic joint location and anisotropic velocity inversion for hydraulic fracturing in a tight Bakken reservoir: Geophysics, **79**, no. 5, C111–C122, doi: 10.1190/geo2013-0345.1.

Maxwell, S., 2009, Microseismic location uncertainty: CSEG Recorder, **34**, 41–46.

Maxwell, S., 2010, Microseismic: Growth born from success: The Leading Edge, **29**, 338–343, doi: 10.1190/1.3353732.

Maxwell, S., 2014, Microseismic imaging of hydraulic fracturing: Improved engineering of unconventional shale reservoirs: SEG.

Maxwell, S., J. Rutledge, R. Jones, and M. Fehler, 2010, Petroleum reservoir characterization using downhole microseismic monitoring: Geophysics, **75**, no. 5, 75A129–175A137, doi: 10.1190/1.3477966.

Miller, R. G., 1974, The jackknife — A review: Biometrika, **61**, 1–15, doi: 10.1093/biomet/61.1.1.

Nava, M. J., J. W. Rector, and Z. Zhang, 2015, Characterization of microseismic source mechanism in the Marcellus shale through analysis in the spectral domain: 85th Annual International Meeting, SEG, Expanded Abstracts, 5069–5073.

Parra, J., C. Hackert, P.-C. Xu, and H. A. Collier, 2006, Attenuation analysis of acoustic waveforms in a borehole intercepted by a sand-shale sequence reservoir: The Leading Edge, **25**, 186–193, doi: 10.1190/1.2172311.

Parra, J. O., C. L. Hackert, A. W. Gorody, and V. Korneev, 2002, Detection of guided waves between gas wells for reservoir characterization: Geophysics, **67**, 38–49, doi: 10.1190/1.1451322.

Petersson, N. A., and B. Sjogreen, 2013, User's guide to SW4, version 1.0: LLNL-SM-xxyy: Lawrence Livermore National Laboratory.

Rutledge, J. T., and W. S. Phillips, 2003, Hydraulic stimulation of natural fractures as revealed by induced microearthquakes, Carthage Cotton Valley gas field, east Texas: Geophysics, **68**, 441–452, doi: 10.1190/1.1567214.

Sleefe, G. E., N. R. Warpinski, and B. P. Engler, 1995, The use of broadband microseisms for hydraulic fracture mapping: SPE Formation Evaluation, **10**, 233–239, doi: 10.2118/26485-PA.

Song, F., and M. N. Toksöz, 2011, Full-waveform based complete moment tensor inversion and source parameter estimation from downhole microseismic data for hydrofracture monitoring: Geophysics, **76**, no. 6, WC103–WC116, doi: 10.1190/geo2011-0027.1.

Warpinski, N., 2009, Microseismic monitoring: Inside and out: Journal of Petroleum Technology, **61**, 80–85, doi: 10.2118/118537-JPT.

Warpinski, N., R. C. Kramm, J. R. Heinze, and C. K. Waltman, 2005, Comparison of single-and dual-array microseismic mapping techniques in the barnett shale: Presented at the SPE Annual Technical Conference and Exhibition, SPE 95568-MS, doi: 10.2118/95568-MS.

Wilson, S., D. Raymer, and R. Jones, 2003, The effects of velocity structure on microseismic location estimates: A case study: 73rd Annual International Meeting, SEG, Expanded Abstracts, 1565–1568.

Yilmaz, Ö., 2001, Seismic data analysis: Processing, inversion, and interpretation of seismic data: SEG.

Yuan, D., and A. Li, 2016, Determination of microseismic event back azimuth from S-wave splitting analysis: 86th Annual International Meeting, SEG, Expanded Abstracts, 2667–2671.

Yuan, D., and A. Li, 2017, Joint inversion for effective anisotropic velocity model and event locations using S-wave splitting measurements from downhole microseismic data: Geophysics, **82**, no. 3, C133–C143, doi: 10.1190/geo2016-0221.1.

Zhang, Z., M. Nava, and J. Rector, 2016, Resonance in downhole microseismic data and its removal: 86th Annual International Meeting, SEG, Expanded Abstracts, 2652–2656.

Zhang, Z., J. W. Rector, and M. J. Nava, 2015, Improving microseismic event location accuracy with head wave arrival time: Case study using Marcellus shale: 85th Annual International Meeting, SEG, Expanded Abstracts, 2473–2478.

Zhang, Z., J. W. Rector, and M. J. Nava, 2017, Simultaneous inversion of multiple microseismic data for event locations and velocity model with Bayesian inference: Geophysics, **82**, no. 3, KS27–KS39, doi: 10.1190/geo2016-0158.1.

Zimmer, U., 2010, Localization of microseismic events using headwaves and direct waves: 80th Annual International Meeting, SEG, Expanded Abstracts, 2196–2200.

Zimmer, U., 2011, Microseismic design studies: Geophysics, **76**, no. 6, WC17–WC25, doi: 10.1190/geo2011-0004.1.